ENG. Struct. Civ. Eng.
https://doi.org/10.1007/s11709-026-1346-0

RESEARCH ARTICLE

Investigation of minimum preload in Rocking Steel Interconnections for sliding prevention

Babak ATASHFARAZ[a], Pejman SHARAFI[a,b*], Ehsan NOROOZINEJAD FARASANGI[c], Kamyar KILDASHTI[a,c]

[a] *Faculty of Engineering, Computing and Science, School of Built Environment and Design, Western Sydney University, Penrith 2751, Australia*

[b] *ARC Industry Transformation Centre for Net Zero Building Platforms (NØBEL), Faculty of Engineering, Computing, and Science, Western Sydney University, Penrith 2751, Australia*

[c] *Urban Transformations Research Centre, Western Sydney University, Penrith 2751, Australia*

[*] *Corresponding author. E-mail: p.sharafi@westernsydney.edu.au*

© The Author(s) 2026.

ABSTRACT The interconnection of modules in corner-supported modular systems is critical for both construction efficiency and structural performance, particularly with respect to shear behaviour. The Rocking Steel Interconnection (RSI) is designed to maintain stability through pretension in its central rod for Prefabricated Prefinished Volumetric Construction (PPVC). Previous studies on the flexural behaviour of the RSI revealed load degradation in the rod and out-of-plane deformation in the lower endplate. These issues may impair the shear performance of the RSI that is studied in this paper using full-scale experimental testing and numerical modelling. A cyclic test was conducted on a full-scale RSI joint with a thicker endplate and a reduced preload in the rod. The aim was to identify the minimum preload required to prevent sliding. Nonlinear Finite Element models were then developed in ABAQUS to validate the experimental results and assess the influence of axial load along with preload. The results show that increasing endplate thickness significantly reduces out-of-plane deformation. Sliding was observed in the final loading cycle. However, axial load from gravity and live loads, combined with sufficient preload, increased frictional resistance to lateral movement. This interaction enhanced the shear performance of the RSI.

KEYWORDS PPVC, corner supported modular frames, moment resisting frame, offsite manufacturing, industrialised construction, RSI, post-tension inter-module connection, sliding

1 Introduction

Prefabricated Prefinished Volumetric Construction (PPVC) is the highest level of prefabrication in the construction industry, providing substantial opportunities to improve the quality, efficiency and digitalisation of building processes [1–3]. In self-supported PPVCs, each module can bear load independently by the shear walls or moment-resisting frames and the load between modules are transferred by interconnections [3–5]. Furthermore, interconnections play a key role in rapid, straightforward assembly and disassembly.

Several models of interconnections have been developed, as reviewed in Refs. [6–8]. Interconnections can be required casting or welding [9–11], which needs on-site work. Multi-bolt interconnections are another type of interconnection in which two parts of adjacent modules are bolted together such as column-to-column [12,13], beam-to-beam [14–17], plate-to-plate [18–21]. Furthermore, some interconnections are assembled by using a single tensile element positioned at the centre of columns [22–26]. A single tensile element in the centre of a column can be an interlock system or a bolt. Although the interlock connection does not require specific access, the large number of components adds complexity to the interconnection [23,27]. On the other hand, a single bolt is a simple concept in which the end plates of the upper and lower columns are fastened together, as shown in Refs. [28,29]. There are different methods for accessing the centre of the column for bolting, such as providing an

Article history: Received Oct 5, 2025; Accepted Dec 21, 2025

access hole [30] or fastening from the top of the column with a long wrench [28]. For practical considerations, the endplate's hole should be wider. In these types of interconnections, the applied shear load may cause the endplates to slide until the bolt body contacts the hole surfaces. To prevent undesirable sliding at the interconnection, the preload can be applied to the tensile element [31,32]. Therefore, Sanches et al. [33] developed a post-tension interconnection utilising a threaded rod placed at the centre of the column. The application of preload on the rod facilitated shear resistance in the connection via friction. However, this interconnection became impractical due to the lack of access to the bolt inside the column. Subsequently, Lacey et al. enhanced the design by incorporating access holes in the column [34]. The shear behaviour of this post-tensioned interconnection was analysed, showing that negligible shear displacement occurred in the connection. Lacey et al. proposed formulas to estimate the overall behaviour of the frictional interconnection under various loading combinations [35].

Another type of interconnections that shear behaviour relies on frictional resistance has been developed by Lee et al. [36]. A long rod of the upper module is fastened to the coupler, and the other side of the coupler is bolted to the lower module's rod. However, the rod of each storey works independently [37]. Another innovative frictional interconnection, named the Rocking Steel Interconnection (RSI) [38], utilises a post-tensioned rod to connect the upper to the lower modules. A packer plate is a horizontal interconnection installed at the lower endplates of the lower modules to cover adjacent columns. After positioning the upper modules onto the packer plate, the rod from the lower module is inserted through the holes and appears from the access hole in the upper module, as shown in Fig. 1. The rod is then fastened to the bearing plate. A hydraulic jack applies preload to the bolt to produce shear resistance between the contact surfaces [39].

The components of RSI, including the collar, spigot, and horizontal plates (end plates, continuity plates, and a bearing plate), which form the structural backbone of the interconnection, as illustrated in Fig. 1. The lower endplate with a nut welded to it, together with a rod, is used on the upper side of the interconnection, as depicted in Fig. 1. After interconnection, the intra-connections, including the rigid floor beam to column connections and the simple ceiling beam to column connections, are installed [39]. The intra-connections are designed in accordance with ANSI/AISC 358-22 [40]. Both rigid and

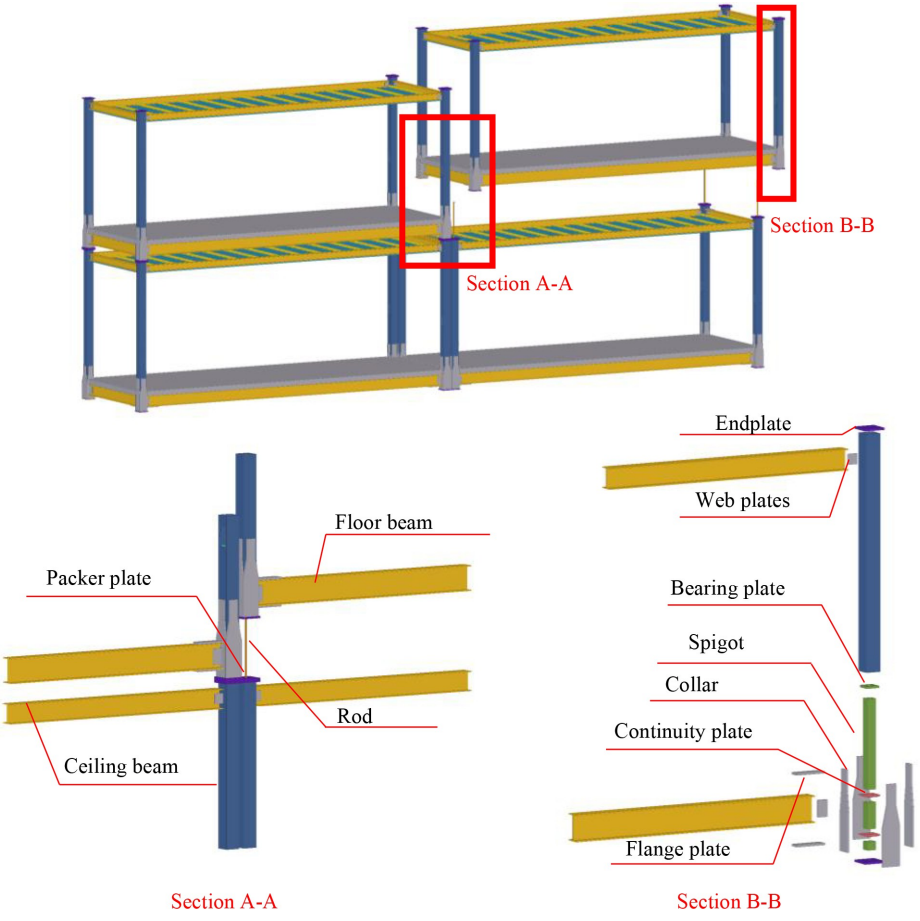


Fig. 1 RSI in a PPVC.

straightforward connections are permitted for this purpose. There are no specific limitations for interconnection in the standards of ANSI/AISC 360-22 [41] and AS 4100-1998 [42]. However, the design guidelines for intra-connections and corresponding limitations are considered in the RSI design, including rigid panel zones owing to the continuity plates.

One of the main challenges in the RSI is the out-of-plane deformation behaviour observed when a thinner endplate is used [38]. This undesirable deformation is also exhibited in an interconnection due to the pull-out load of the single bolt [43]. To address this concern, an investigation is necessary. For this purpose, the current paper aims to assess the effects of endplate thickness on joint performance.

The shear behaviour of the interconnection is essential for mitigating lateral movements of modules (sliding) under different conditions, such as wind loads [31], seismic events [44,45], and progressive collapse scenarios [46–48]. The shear behaviour of the RSI is affected by the frictional resistance between the endplates, which relies on both axial loads and preload. A decrease in axial load and preload may result in sliding due to reduced frictional resistance. The load degradation of the rod was observed in the study by Atashfaraz et al. [38] which can reduce the reliability of the RSI in shear behaviour and lead to interconnection sliding at significant drift. However, it is preferable to prevent any sliding at the system joint and ensure the joint fails by creating a plastic hinge at the connection.

This paper determines the minimum preload required to prevent sliding, considering load degradation in the rod. For this purpose, in the initial phase, the frictional coefficient was measured through the test. Then, a full-scale test was performed applying the minimum preload required to prevent sliding. Meanwhile, the thickness of the specimen's endplate is increased to prevent out-of-plane deformation of the plate, which can occur due to the rod's pull-out load. A numerical analysis was conducted using ABAQUS [49] to investigate the effects of load degradation and out-of-plane deformation on the shear behaviour of RSI. Additionally, the shear and general behaviour of the joint were studied when various axial loads at the top of the column were imposed.

2 Shear behaviour of the Rocking Steel Interconnection

In the RSI, the shear load from the upper storey is transmitted to the lower storey through the contact surfaces of the endplates. The shear behaviour of an RSI is depicted in Fig. 2 obtained from a shear test on two plates [50,51]. According to Fig. 2, when the applied shear load exceeds the frictional resistance, the plates slide until the rod's body comes into contact with the hole surface. Following this collision, the shear response exhibits a sharp increase, which subsequently levels off as the bolt ultimately yields in shear, as shown yielding phase by dash line in Fig. 2.

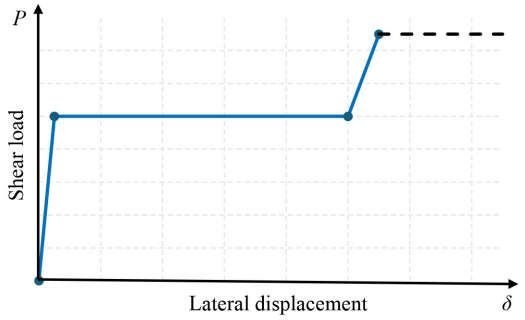


Fig. 2 Shear load–lateral displacement of bolted plates [50].

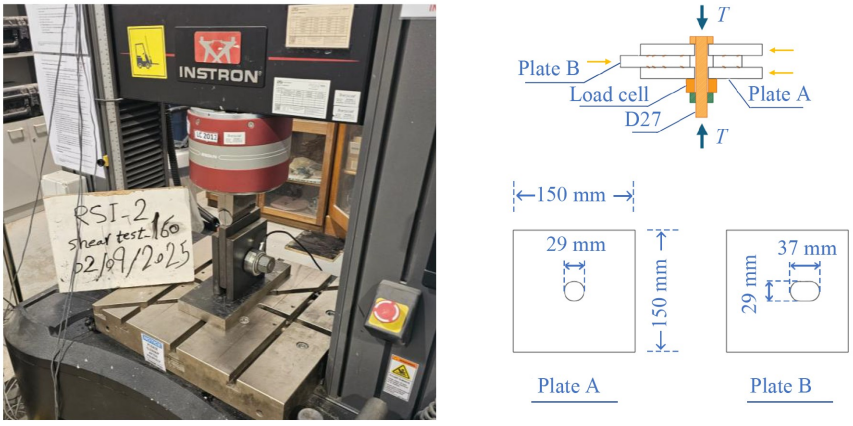
The frictional resistance must be sufficient to prevent sliding, as any sliding can result in collision and consequently induce additional tensile stresses in the rod. Ideally, the rod is supposed to resist only the tensile forces due to the moment in the RSI.

Additionally, the RSI is designed to have a flexural failure mode, characterised by the formation of a plastic hinge within the RSI or the beam [38]. To prevent sliding, which can compromise the building's structural stability, the shear resistance of the RSI must exceed the shear load imposed by the column. The shear resistance of RSI depends on the loads and the coefficient of friction between the plates.

A shear test was conducted to determine the coefficient of friction between the endplate surfaces (Fig. 3). A bolt with a 26 mm diameter was post-tensioned to 160 kN to provide axial load and create friction between the plates. The bolt connected two side plates (Plate A), and the middle plate (Plate B), which contained a bean-shaped hole as shown in Fig. 3. Plates A were sited on the Universal Testing Machine (UTM) bed while Plate B was free to slide downward under the applied compressive load.

After sliding, the load remained nearly constant (Fig. 4). When the bolt contacted the hole of Plate B, the load increased sharply. The test was stopped due to the capacity limit of the UTM. The objective of this test was to determine the frictional coefficient, calculated as the ratio of the sliding load to the axial load. Based on Fig. 4, the measured frictional coefficient between the endplates is 0.38, which can be used in shear behaviour calculations.

The axial load in an RSI is derived from the preload, applied moment, and gravity loads. To estimate this load, a structure incorporating RSIs was designed and analysed in Ref. [39]. Gravity loads from dead and live loads in the RSIs of a 12-storey building in Ref. [39] are adopted in this study. However, the moment and preload values are variable. To examine the relationship between shear load



(a) (b)

Fig. 3 (a) Shear test between the endplates of RSI; (b) the elevation view of the sample.

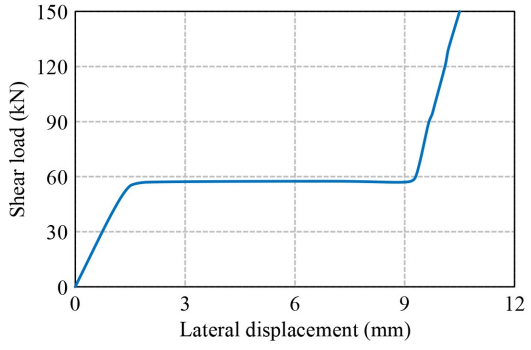


Fig. 4 Shear load–lateral displacement between plates.

and bending moment in an RSI, a three-storey frame was analysed under a static pushover load using ETABS. The resulting moment and shear diagrams are shown in Fig. 5.

The joint involves a rigid floor beam-to-column connection. Additionally, the frame includes ceiling beams with a simple connection that cannot withstand significant moments. Hence, the existence of the ceiling beam was ignored in the analysis due to the simplification. It should be noted that the ceiling beam of the top floor is considered rigid to ensure a stable frame.

Interconnections are characterised as links that connect columns. To simplify the calculation, the bilinear behaviour derived from the test results in the previous work [39] was utilised for the moment behaviour of RSI. Furthermore, it is assumed that the RSI has shear rigidity due to frictional resistance and that it behaves perfectly rigid in shear.

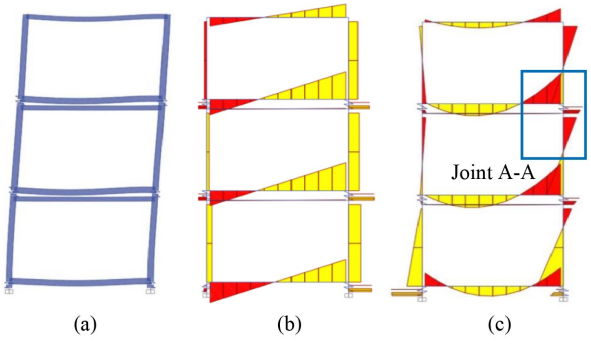


Fig. 5 Diagrams of three-story frame: (a) deformation; (b) shear; (c) moment.

The combination of dead and live loads is imposed on the floor beams in accordance with AS/NZS 1170.0 [52] and AS/NZS 1170.1 [53], whereas static loads are applied in a triangular pattern to the floor beams of each story. The moment and shear distribution diagrams presented in Fig. 5 are obtained from the structural analysis of the frame in its elastic state.

Shear remains constant along the length of the columns, and its value increases with increasing load at the column tip. The moment load at the service state, where no openings exist in the RSI, is calculated by multiplying the shear force (V) by the column length (L_c) at the interconnection for the joint. Additionally, the moment at the ends of the beams (M_b) is the sum of the moments of the column (M_c) connected to the beam and RSI's moment (M_R) in a joint.

By increasing the push load, RSI reaches to the maximum capacity or the yield moment of the beam. In this frame $M_R \leqslant \frac{M_b}{2}$ in which the first plastic hinge is formed in RSI based on Ref. [38]. If the first plastic hinges form in RSI, the value of shear through the column and RSI is Eq. (1):

$$V = \frac{M_P}{L_c} = \frac{M_b - M_c}{L_c}, \tag{1}$$

where M_P is the maximum capacity of RSI.

Forming the first series of plastic hinges in RSIs will not lead to structural instability. The frames will continue to take on more lateral loads until other hinges are formed in either columns or beams. The additional shear required for the second hinge is calculated using Eq. (2). It is supposed that the second plastic forms in the beam due to the column's higher moment capacity compared to that of

the beams ($M_R \leqslant \frac{M_b}{2}$):

$$V' = \frac{M_b - M_P}{L_c}. \quad (2)$$

Sliding does not occur if the shear load in RSI($V + V'$) is lower than the frictional resistance of the RSI(V_f), which is determined by Eq. (3):

$$V_f = \mu(P_G + P_L + V_B + C) + V_{rod}, \quad (3)$$

where μ is the frictional coefficient that is equal to 0.38 based on the frictional test, indicated in Fig. 4. The gravity and live loads (P_G and P_L, respectively) increase the shear resistance of RSI. The insignificant shear resistance of the rod (V_{rod}) is ignored in this calculation.

The value of V_B as the shear of the beam affects the axial load in the column which is considered in Eq. (3). The two ends of a beam have shear forces of V_B in opposite directions. At one end, the positive shear force increases the shear resistance, while at the opposite end, the negative shear force reduces the shear resistance of the RSI. During the test of a non-sway joint, a cyclic load is imposed on the beam, V_B in Eq. (3) appears in the column and RSI.

The bending moment in the RSI connection results from the interaction between the rod, which resists tensile loads, and the endplates, which bear the compressive load (C). The tensile and compressive loads due to the bending moment in an RSI are equal. As the tensile force is more accessible for measurement, it is used instead of C in Eq. (3). Any reduction in the tensile force (due to load degradation in the rod) may have effects on the shear and moment behaviours of RSI. Therefore, it is essential to investigate the shear behaviour through full-scale testing.

3 Experimental programs

An RSI connection that has identical dimensions to those presented in Ref. [38] was built and tested for the evaluation of the shear behaviour. For this test, the rod was subjected to a lower preload, and a thicker lower endplate was used. The primary objectives of this testing scenario were to determine the minimum preload required to prevent sliding and to investigate the effect of endplate out-of-plane deformation on the load degradation of the rod, a phenomenon previously identified in Ref. [38].

3.1 Test specimen

A full-scale specimen, with dimensions shown in Fig. 6, was tested at the University of Western Sydney. In the test setup, the columns and beam were aligned with the strong floor. Square Hollow Sections (SHS) and a Universal Beam (UB) were used for the column and beam, respectively. The selected element sizes were SHS 200 × 200 × 9 for the column and 200UB29.8 for the beam, derived from structural analysis for a 12-story building located in Sydney. The ceiling beam was excluded from this sample due to its simple connection to the columns.

The specimen labelled as C-T2 in this paper was obtained from the previous work [38]. The endplates on both sides of the RSI in C-T2 are rectangular, with dimensions of 262 mm × 262 mm × 20 mm. This paper introduces a newly developed specimen, referred to as

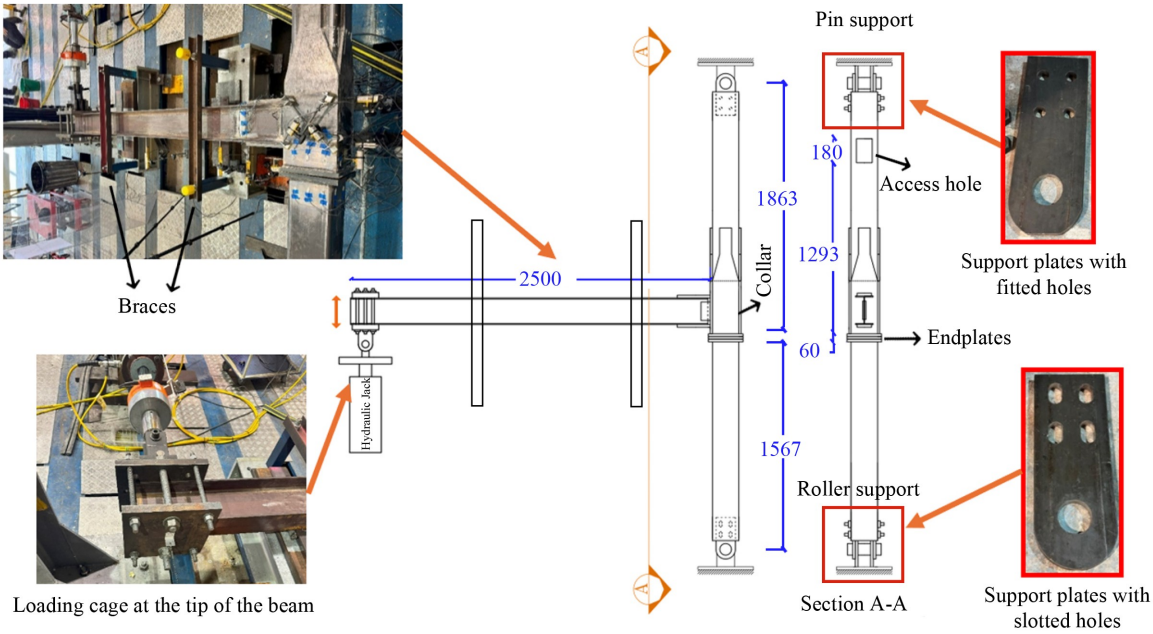


Fig. 6 Test setup and support conditions of C-T3 (unit: mm).

C-T3, which features an upper endplate measuring 262 mm × 262 mm × 20 mm, welded to the collar, and a lower endplate measuring 262 mm × 262 mm × 30 mm, connected to the lower column. This modification is intended to control the out-of-plane deformation observed in C-T2. All components are expected to remain intact, except for the rod, which can be replaced after significant loading to ensure the PPVC system continues to function effectively. A thicker plate may also increase the moment capacity of the connection, as Aryan et al. [54] determined in column end-plate connections.

For both samples, the spigots with sections of SHS 75 mm × 75 mm × 6 mm and 16 mm thick plates for continuity plates and collars were used. The material properties are presented in Ref. [38]. For both specimens, M8.8 rods with a diameter of 27 mm were fastened to the bearing plate to the lower endplate.

In C-T2, a preload of 320 kN was applied to the rod, which decreased to 156 kN at a drift of 5% [38]. This indicates that if the initial preload had been about 160 kN, sliding would be expected to occur at a drift of 5%. For this reason, a preload of 160 kN was applied to the rod in C-T3. Nevertheless, the likelihood of sliding must still be tested, as the influence of out-of-plane deformation on load degradation remains uncertain and the rod experiences the load degradation through unloading when there is less shear load.

The specimen was connected to the rigid floor with a pin support on one side of the column and a roller support on the opposite side. For the pinned support, the plates connecting the column to the rigid floor had fitted holes that prevented any column displacement. In contrast, the plates with slotted holes were utilised for the roller support, which allowed the column to move freely along its length, as illustrated in Fig. 6. The specimen was secured to the floor at the supports; Lateral braces were installed to the beam (Fig. 6) and a hydraulic jack was installed at the beam's free end. Finally, the hydraulic jack was installed at the tip of the beam to set-up the test for the non-sway joint. The beam's tip is fixed in the cage, which is connected by a pin support to the hydraulic jack.

3.2 Loading and instrumentation

Displacements across the specimen were monitored using Linear Variable Differential Transformers (LVDTs), designated L1–L13, as depicted in Fig. 7. A load cell was installed between the nut and the bearing plate to monitor the load during both preloading and testing (Fig. 7). An LVDT (LC1) was installed at the free end of the beam, opposite the loading point. LVDTs L2 and L3 captured the vertical and lateral movements of the RSI end plates, respectively. Two LVDTs, L6 and L7, were installed in the protected zone of the beam. The two diagonal LVDTs, L8 and L9, were installed to measure the shear deformation of the panel zone, while L10 and L11 were positioned parallel to the continuity plates. Furthermore, L4 and L5 were aligned parallel to the column's length and positioned at the supports, as shown in Fig. 7.

In specimen C-T3, 16 strain gauges were installed at critical locations, as shown in Fig. 7. The letter S is used for naming strain gauges. S1–S7 were positioned on the beam, 350 mm from the column surfaces. The remaining

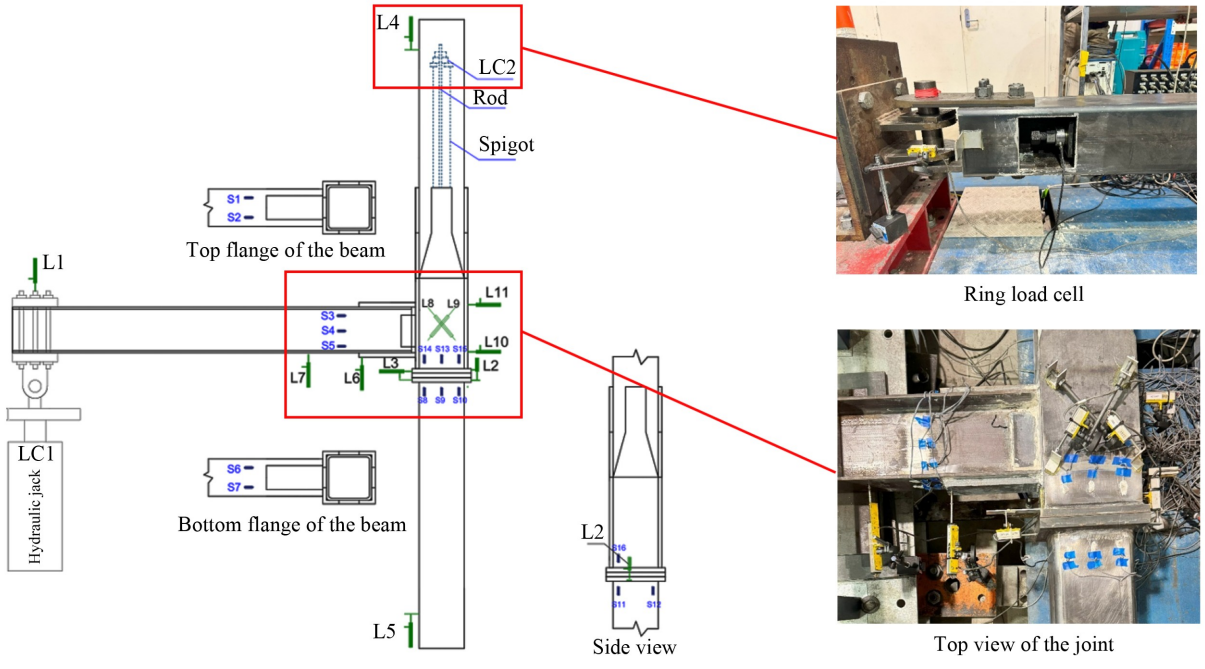


Fig. 7 The places of LVDTs and strain gauges.

strain gauges were installed around the lower column and collars close to the endplates.

The ANSI/AISC 341-16 cyclic test loading protocol in Table 1 was adopted for the testing of the joint [55]. The displacement-control load history includes both elastic and inelastic phases. After 2% drift, which was equal to 50 mm vertical displacement, each cycle incrementally increased by 1% drift. The loading process continued beyond a 5% drift, satisfying the minimum requirement of ANSI/AISC 341-16 for assessing joint behaviour.

Table 1 Loading protocol based on ANSI/AISC 341-16 [55]

Iteration	Drift (%)	Displacement (mm)
6	0.25	8.5
6	0.50	17.0
6	0.75	25.5
4	1.00	34.0
2	1.50	51.0
2	2.00	68.0
2	3.00	102.0
2	4.00	136.0
2	5.00	170.0

3.3 Results and discussion

Figure 8(a) illustrates the moment-rotation behaviour of C-T3, where the moment is calculated by multiplying the applied load shown in Fig. 5(b) by the distance from the column's centre to the loading point. Figure 8(b) indicates that the preload has a negligible influence on the maximum moment capacity, as observed from the load–displacement comparison of specimens C-T3 and C-T2. Stiffness degradation, as demonstrated in Fig. 8(b), starts at an earlier stage in the specimen with a lower preload value (C-T3).

The joint's deformation pattern was seen through four distinct stages: Elastic, opening, sliding, and failure. During the initial stage, the joint exhibited elastic behaviour, with no apparent separation between the endplates. With an increase in the applied load, the second stage commenced at approximately 1.0% drift, characterised by the opening of the joint, as seen in Fig. 9(a). The opening continued to enlarge until the load remained stable in the second stage (Fig. 9(b)). Sliding was observed during the unloading phase at a 6% drift, as displayed in Fig. 9(c). Despite the lateral movement within the RSI, the moment-resisting behaviour of the joint remains unaffected. Due to the hydraulic jack's limitations, the maximum drift of the specimen is reached at 6%. The joint load indicates an 11% reduction in this drift ratio. Therefore, this reduction in the load capacity of the joint is considered as the failure criterion.

The maximum load remained constant up to a 4% drift, after which, at the maximum drift of 6% (the laboratory's limit), the load decreased by 11%. The post-test examination of the disassembled components indicated that all elements were intact, except the rod, which exhibited rotational deformation near its lower endplate. In contrast to sample C-T2, the lower endplate of C-T3 showed no out-of-plane deformation. This indicates that incorporating a thicker plate at the lower endplate significantly reduces damage levels. The rod was easily removed, and the nut welded to the lower endplate experienced no damage. As all components remain intact, the joint's serviceability may be restored by replacing the deformed rod, suggesting the possibility of repair and continued functionality of the connection system.

According to Eq. (4), the scant stiffness of C-T3 and C-T2 is calculated in Table 2. The values indicate a consistent reduction in stiffness. The thickness of the endplate and the preload value cannot affect the overall behaviour of RSI.

$$K_{\mathrm{sec},i} = \frac{|F_i^+| + |F_i^-|}{|\Delta_i^+| + |\Delta_i^-|}, \tag{4}$$

where F_i^+ and F_i^- represent the positive and negative peak loads for each loading cycle (denoted by i), respectively. The corresponding drifts at these peak loads are denoted as Δ_i^+ and Δ_i^-.

The energy dissipated during each loading cycle is represented by the area enclosed within the hysteretic loop. In Fig. 10, the area of each cycle (*SABCD*) corresponds to the energy dissipation calculated for both specimens. As shown in Table 2, a lower preload results in reduced energy dissipation by the joint, particularly during the initial cycles following the opening phase.

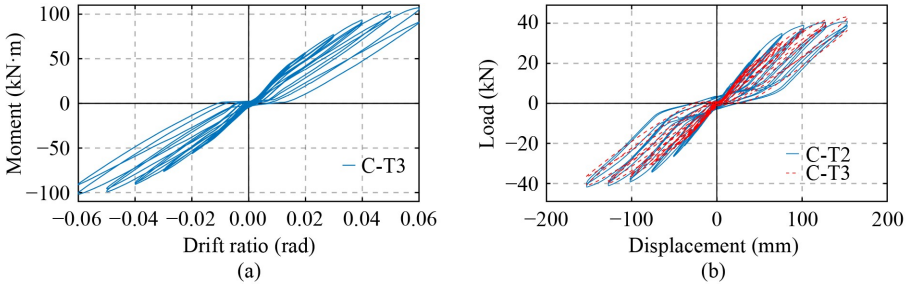


Fig. 8 Test results: (a) moment–drift; (b) load–tip beam displacement.

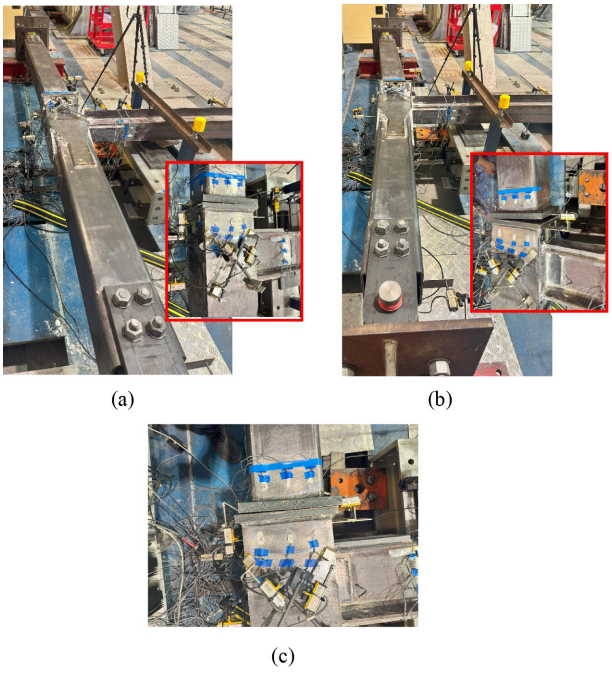


Fig. 9 Deformation of RSI in the status of (a) opening; (b) large opening; (c) sliding.

The support conditions were assumed to consist of a roller on one side and a pin on the other side. Figure 11 represents the displacements recorded by L4 and L5. The displacement of the pin support, as monitored by L4, indicates that it experienced some minimal movement due to experimental errors, which need to be considered during the verification process.

The data from the strain gauges on the beam flanges are presented in Fig. 12. It shows that the strain of the beam's protected zone remained within the elastic range. The maximum strain values in the beam were similar to those observed in C-T2. Consequently, the beam's load capacity appears unaffected by the preload value and the thickness of the endplate.

The lower column region at the weld joint with the endplate requires more attention. This area was monitored using strain gauges (S8 to S12) attached to the lower column, whereas strain gauges S13 to S16 were positioned on the collar near the upper endplate.

Figure 13(a) indicates that the corners of the lower column experienced increased tension compared to the middle of the column's web. Two strain gauges placed on the lower column flange (S11 and S12) recorded the maximum values when the compressive zone appeared on that side (Fig. 13(b)). If the RSI on that side experienced an uplift, the strain values became positive, indicating that the flange was subjected to tensile forces due to the pull-out load of the rod.

Figure 13 reveals that the strain on the lower side of the RSI decreased significantly with the implementation of a thicker endplate compared to the C-T2 sample. A comparison of the strain in Fig. 13 indicates that the thicker plate distributes better both the tensile loads from rod pull-out and the compressive loads induced by the couple moment on the lower endplate's side.

The upper side of the RSI exhibited negligible tension, attributable to the substantial rigidity provided by the thicker collar, as illustrated in Fig. 14. The maximum strain recorded by S16 on the collar was approximately one-third of that measured by S10 on the lower part, located at the same position on both sides of the endplates.

Figure 15 illustrates the diagonal strain of the panel zones. This observation highlights the panel zone's high rigidity, attributed to minimal shear deformation in this area of the column. Additionally, all components of intra-connections, such as web and flange plates, did not experience any plastic deformation. These features indicate that the joint meets the requirements for a prequalified intra-connection in accordance with ANSI/AISC 358-22 standards [40]. In this way, the intra-connection through the structural analysis can be considered the ideal rigid.

The width of the opening of one side in Fig. 16 was zero when that side was within the compressive zone. The width gradually expanded, with the rate of opening rising from approximately 1% drift, as measured by the L2. The initial opening was distinguished at approximately 2% drift during the test. At the final step of 5% increment, a 2 mm deformation was observed (Fig. 16), which was attributed to experimental errors arising from the instability and separation of the LVDT during the final cycles.

Table 2 Parameters of each drift for specimens

Drift (%)	C-T3			C-T2		
	$S_{ABCD,\ area}$ (kN·m)	$S_{\Delta ODF,\ area}$ (kN·m)	K_{sec} (kN/mm)	$S_{ABCD,\ area}$ (kN·m)	$S_{\Delta ODF,\ area}$ (kN·m)	K_{sec} (kN/mm)
1.0	34	330	5.12	56	370	5.48
1.5	96	703	4.81	110	800	5.23
2.0	173	1160	4.78	200	1400	5.16
3.0	475	2369	4.05	610	2600	4.55
4.0	906	3792	3.55	1200	4000	3.85
5.0	1602	5207	3.20	1700	5200	3.22
6.0	2136	6452	2.41	2100	6300	2.71

Figure 17 illustrates the lateral displacements of the two endplates as measured by the L3 measurement. Figure 17 confirms that sliding movement occurred at a drift of 6%, as seen in the numerical program. According to AISC 360-22 [41], the behaviour of the connection till a drift of 5% is considered, as the RSI did not have any sliding. However, the test was conducted under ideal conditions in which preload relaxation did not affect the initial preload. Therefore, the minimum preload for this joint is 165 kN. If the value is lower than this, there is a risk of sliding at an earlier stage, indicating that the building is

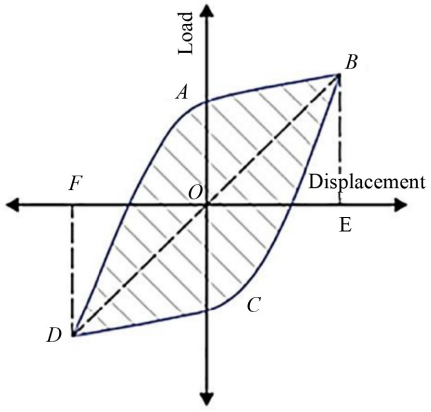


Fig. 10 Energy dissipation from push behaviour.

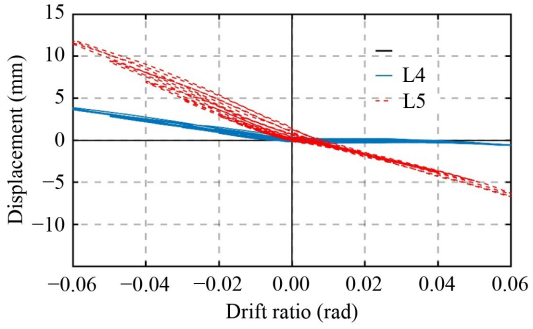


Fig. 11 Support movements during the test.

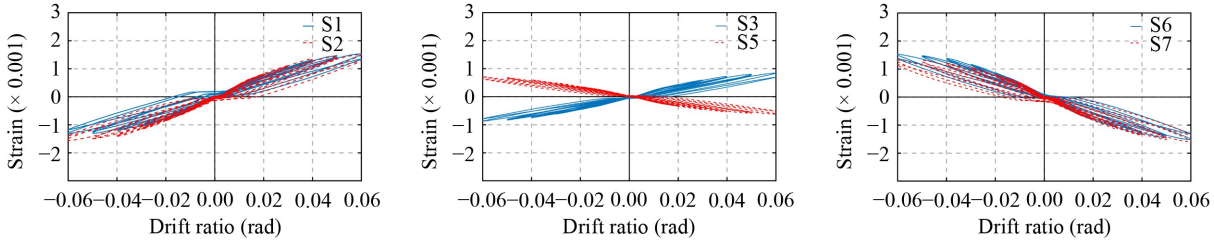


Fig. 12 Strains of the protected zone of the beam.

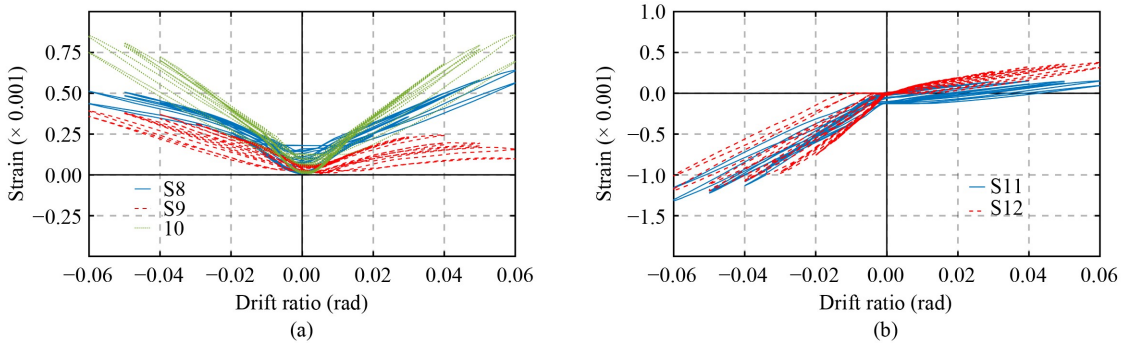


Fig. 13 The strain values around the lower endplate of C-T3.

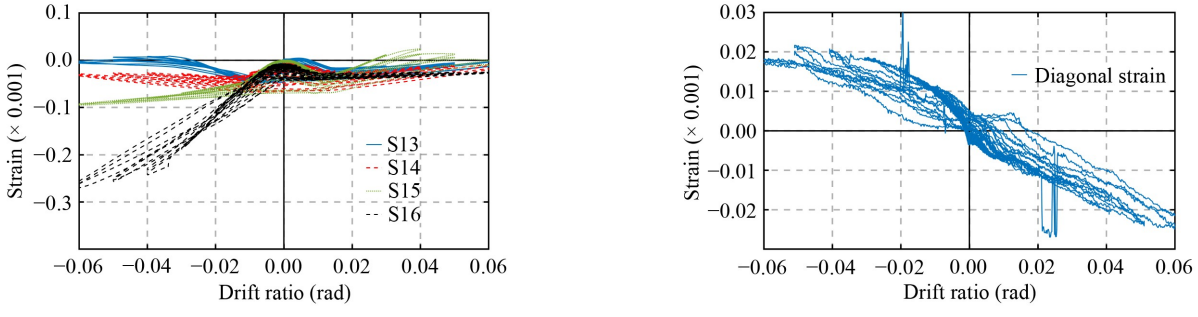


Fig. 14 Strain of the upper side of RSI in C-T3.

Fig. 15 Diagonal strain of the panel zone.

unstable.

Figure 18 displays the monitored load at the rod's head. The initial load for C-T3 was 162 kN. The preload remained consistent as the sample's drift reached zero and continued until the first opening occurred. Subsequently, load degradation was noted as the drift increased due to residual deformation. The rod reached its capacity as the opening expanded to its maximum drift at each cycle. However, during unloading, as the gap closed, the preload decreased from its initial value due to residual stress. The effect of out-of-plane deformation of the lower endplate on load degradation remains unclear; however, it can be determined through finite-element analysis.

Table 3 shows the load values in each cycle to be used in Eq. (3). The reported values for 1% drift in each cycle are based on the loads at the time of unloading, where the shear load exceeds the shear resistance of the RSI at the last drift. In fact, when the RSI experiences the maximum drift of the cycle, there is no likelihood of sliding because the rod's load reaches the maximum value shown in Fig. 17. For this reason, the unloading condition is prone to sliding. At the last drift (6%), the trend of load degradation flattened and coincided with the onset of sliding. The moment value in the RSI at a drift ratio of 0% was close to zero, indicating no significant compressive load. The preload and shear values recorded at the onset of sliding were approximately 6.7 and 2.75 kN, respectively. The shear resistance of the RSI, calculated using Eq. (3), was about 2.65 kN, which is lower than the shear demand in the RSI when assuming a Coulomb friction coefficient of 0.38. As a result, the applied shear load exceeded the shear resistance specified by Eq. (3), leading to sliding within the RSI. The lower components continued sliding until the rod's surface contacted the hole's surface.

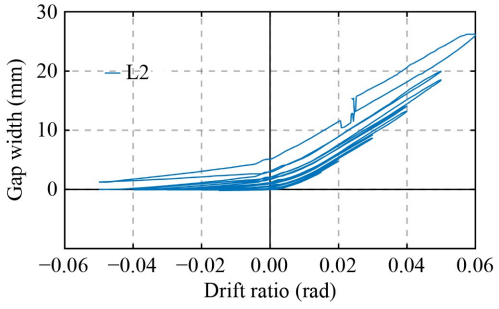


Fig. 16 The width of the opening around a side.

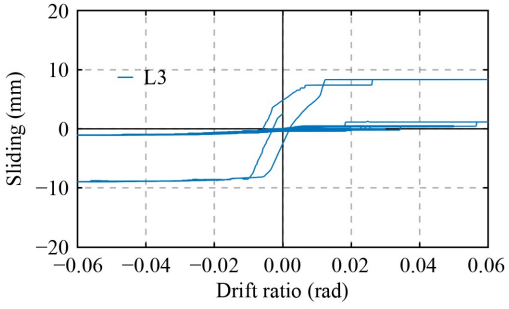


Fig. 17 Sliding displacement of RSI.

4 Numerical programs

In this section, the Finite Element (FE) model of the tested joint was simulated using ABAQUS to further examine the joint's behaviour, including load degradation in the rod and deformation of the endplate.

4.1 Finite Element models

In ABAQUS, steel is modelled using an elastic−plastic formulation, incorporating properties listed in Table 4. A combined-hardening model as proposed by Ban and Shi [56] was introduced for steel profiles and plates, while

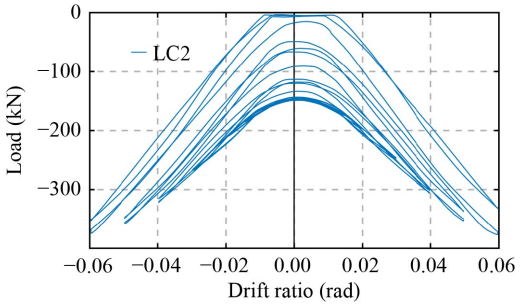


Fig. 18 Monitored load of the rod.

Table 3 Loads and moments of C-T3 in drifts

Drift (%)	M_{max} (kN·m)	V_{max} (kN)	$M_{1\%}$ (kN·m)	$V_{1\%}$ (kN)	T_{max} (kN)	T_{min} (kN)	$T_{1\%}$ (kN)
1.0	42	13	37	11	176	165	173
1.5	55	17	27	8	189	165	173
2.0	77	24	25	7	192	162	173
3.0	92	28	21	6	212	150	155
4.0	102	31	16	5	262	133	146
5.0	107	33	8	3	308	86	102
6.0	96	30	< 1	2	378	7	7

Table 4 Material properties

Component	Steel grade	Thickness (mm)	Yield stress (MPa)	Tensile stress (MPa)	Elastic modules (GPa)
Steel hollow section	C350	8.9	342	425	198
Steel UB section	C300	9	311	450	201
Collars' plate	C350	16	356	440	199
M27 threaded rod	Class 8.8	–	–	820	–

kinematic hardening was used for rod properties. The yield strength and ultimate strength were defined based on the coupon tests presented in Table 4.

The butt weld length between the two components was modelled using tie constraints. To model the fillet weld between the lower column and the end plate, a thin, high-rigidity strip was introduced around the lower column to connect to the lower end plate. One side of the strip is tied to the outside surface of the column, and the other side is tied to the endplate, similar to a fillet weld, which can affect the plate's boundary condition, as determined in Ref. [38]. Surface-to-surface contact was used between surfaces that have frictional contact, such as endplates. This contact model uses Coulomb friction, with a penalty-based formulation and hard contact in normal behaviour. A friction coefficient of 0.38, as discussed in Section 2, was adopted in the models.

To ensure an accurate representation of the shear behaviour, the RSI was modelled, as displayed in Fig. 19. A lateral push-over static load was applied to the top endplate, while the lower endplate was fully restrained in all degrees of freedom. Lateral loads can be applied at the tips of walls, as modelled in Ref. [57], to study shear behaviour. However, if the lateral load is applied to the tip of the model in Fig. 18, it is possible that rocking affects the shear results. Hence, the point of lateral displacement was located close to the contact surface, thereby ensuring that the models acted predominantly in shear.

In the following, the behaviour of the joint was studied under cyclic loading with axial load. The loading protocol [55] was imposed on the tip of the beam in Fig. 20, and

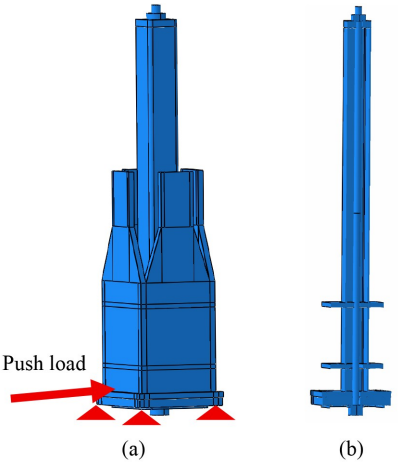


Fig. 19 (a) Model for assessing the shear behaviour; (b) section view of the model.

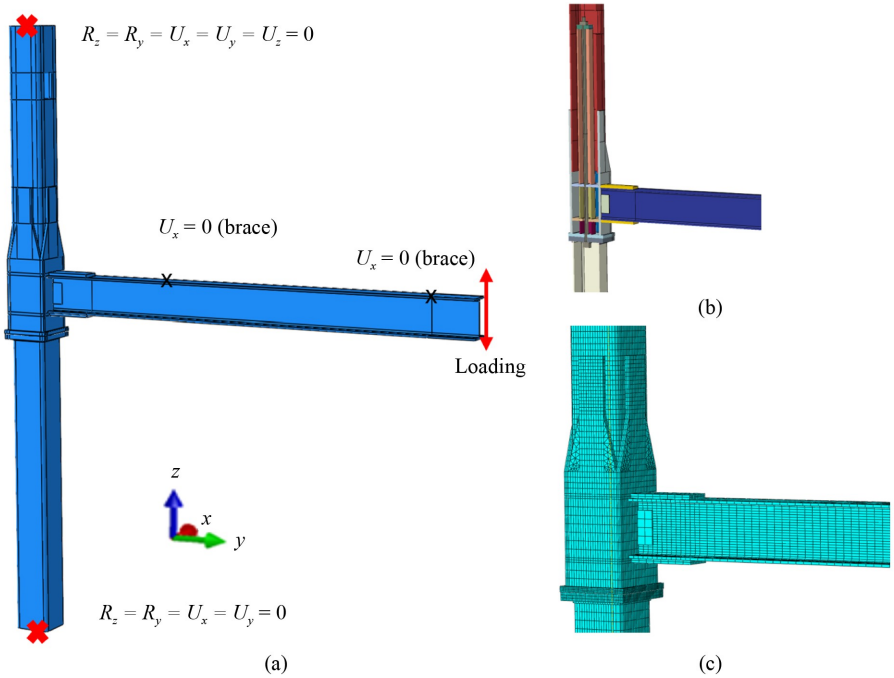


Fig. 20 (a) Boundary conditions; (b) components inside of the column; (c) mesh sample of FE models.

the U_x translational degree of the beam's end section was constrained. Additionally, the support of the upper column in all the translational degrees of a reference point was restrained as pinned support. The roller support was provided for the lower column, in which the transitional degrees, except the z direction, were restrained, as shown in the boundary conditions in Fig. 20. During verification, the movements of pinned support along the length of the column, presented in Fig. 11, were defined in the model. The displacements did not affect the results compared to the ideal condition. Therefore, this error was ignored in the modelling.

To investigate the out-of-plane deformation of endplates and the influence of boundary conditions, specific models involve a 20-mm-thick endplate [38], referred to as 'T2', while others have thicker endplates of 30 mm, labelled as 'T3'. Some models have collars for both sides of the RSI, denoted by a 'C' at the beginning of their names.

In order to recognise the importance of preload, 60% and 30% of the rod's tensile strength were applied to the sample. The P3 and P1.5 in the names represent the percentage of imposed load, which are 320 and 160 kN, respectively, for the 27-mm-diameter rod.

Axial load increases the shear capacity of the connection. It may also enhance the moment capacity, as Wang et al. observed in channel steel-bolt joints [58]. An axial load, which may affect the overall behaviour of the connection, was applied in some models. The axial load due to the combination of gravity and live loads can be 610 kN in a twelve-story building, and this value reduces in the columns of the upper stories. The axial load in model 'A20' is 640 kN, indicating a severe scenario in the structure. The axial load percentages of 5% and 10% of the column's compressive strength were designated as models A5 and A10, respectively. Six models were studied at four different axial load levels, yielding a total of 24 models, as presented in Table 5. The T3-1.5-A0 model, similar to the experimental sample, was developed with a 30 mm-thick endplate and a rod under a preload of 160 kN. This paper used the experimental and FE models of T2-3-A0 as reported by Ref. [38].

The FE model was developed using C3D8RI solid elements, with mesh sizes adjusted based on the numerical convergence analysis. The size of the mesh is shown in Fig. 20, and the sensitive analysis of meshes is reported in Ref. [38]. The Newton-Raphson solver in the ABAQUS/Standard module was used to perform an implicit static analysis.

4.2 Results and discussion

At the initial stage, the frictional behaviour of the model in Fig. 19 under purified shear load is examined. Figure 21 presents the shear response of the connection subjected to shear loading. As discussed in Section 2, three distinct stages are observed in Fig. 21: frictional resistance, sliding, and bolt resistance.

The upper part of the RSI in the model for assessing shear behaviour (Fig. 19) resists a considerable shear load with high stiffness until sliding initiates. Thereafter, the top part slides on the lower endplate by approximately 9 mm (Fig. 22(a)) with only a marginal increase in shear load. Once the rod body contacts the hole surface, shear resistance increases sharply. This contact generates great stresses at the end length of the rod, as depicted by von Mises stress in Fig. 22(b).

The interconnection is subjected to combined shear and moment effects. The compressive force induced by the moment enhances shear resistance, as expressed in Eq. (3). To determine the actual joint behaviour, a full-scale model should be analysed, with the friction coefficient between the surfaces assumed to be 0.38.

The FE model T3-P1.5-A0 matches perfectly with the experimental data based on Fig. 23. During the loading of the model T3-P1.5-A0, four steps appeared similar to the experiment: elastic, opening, sliding, and failure. After elastic status, the gap between endplates started to open from drift by 1% (Fig. 24(a)). Sliding occurred through unloading at a drift of 6% (Fig. 24(b)), as observed through the experimental test. Finally, the rod exhibited greater residual deformation near the endplate, as shown in Fig. 24(c), which caused failure. According to the von Mises stress in Fig. 24, the beam-to-column connection experiences elastic stress in the panel zone and in the components that connect the beam to the column, and the high stress in the beam occurs in the protected zone, which is far from the column's surface at about the length of the flange plates. As a result, it indicates that the prequalified intra-connection meets the requirements of

Table 5 The properties and loading of models

Model	Lower plate (mm)	Preload (kN)	Axial load (kN)
T3-P1.5-A[0, 5, 10, 20]	30	160	[0, 160, 320, 640]
T2-P1.5-A[0, 5, 10, 20]	20	160	[0, 160, 320, 640]
C-P1.5-A[0, 5, 10, 20]	20*	160	[0, 160, 320, 640]
T3-P3-A[0, 5, 10, 20]	30	320	[0, 160, 320, 640]
T2-P3-A[0, 5, 10, 20]	20	320	[0, 160, 320, 640]
C-P3-A[0, 5, 10, 20]	20*	320	[0, 160, 320, 640]

Note: *This model involves the lower column.

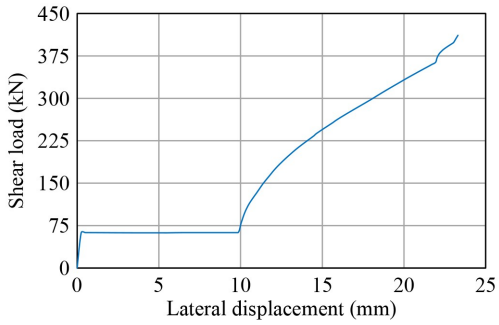


Fig. 21 The purified shear behaviour of RSI.

ANSI/AISC 358-22 [40].

The thickness of the endplate does not have an effect on the general behaviour of the joint. The model T2-P1.5-A0, consisting of a plate with a thickness of 20 mm, exhibits a behaviour like that of model T3-P1.5-A0. However, there was no sliding between the endplates of model T2-P1.5-A0 caused by the out-of-plane deformation in the lower endplate. Furthermore, model C-P1.5-A0 has no significant effect on the results, and the behaviour remains comparable to that of T3-P1.5-A0 despite the convergence issues at the last drifts.

The axial load of the rod in Fig. 18, was compared with the FE result in Fig. 25(a), which approves the acceptable compliance. When the cycle's drift reaches the maximum displacement, the rod works at the maximum capacity, as seen in Fig. 25(a). The interaction of the rod and the end plate subsequently provides the maximum moment of RSI regardless of the preload value and the thickness of the end plate.

On the other hand, when the displacement approaches zero drift, the load degradation causes the preload value in the rod to decrease below its initial value. The load degradation in the rod begins at approximately 1% drift when the opening appears in model T3-P1.5-A0, as shown in Fig. 25(b).

Load degradation in the rod of 'T3-P1.5-A0' reduces the total compressive load on the RSI contact surface below the required threshold to prevent sliding. The numerical results confirm sliding at a 6% drift, as the frictional resistance becomes lower than the shear load through the column. The values of frictional resistance and shear load through the RSI at the point where sliding occurred are about 3.2 and 4.5 kN, respectively.

Lateral movement is influenced by the distance between the rod's surface and the hole. The lower part of the RSI continues to move until the rod and hole surfaces of the upper endplate make contact. Although the interaction of the rod with the hole's surface may increase 'V_{rod}' in Eq. (3), the contact may induce additional tension in the rod's body, which can be ignored in static analysis.

The existence of the ceiling beam was ignored in all experimental and numerical models when it had simple beam-to-column connections. There are two reasons for this issue: the connection is considered to be an ideal pinned connection through the structural analysis, and the insignificant moment due to the ceiling beam's connection does not have an effect on the joint's behaviour.

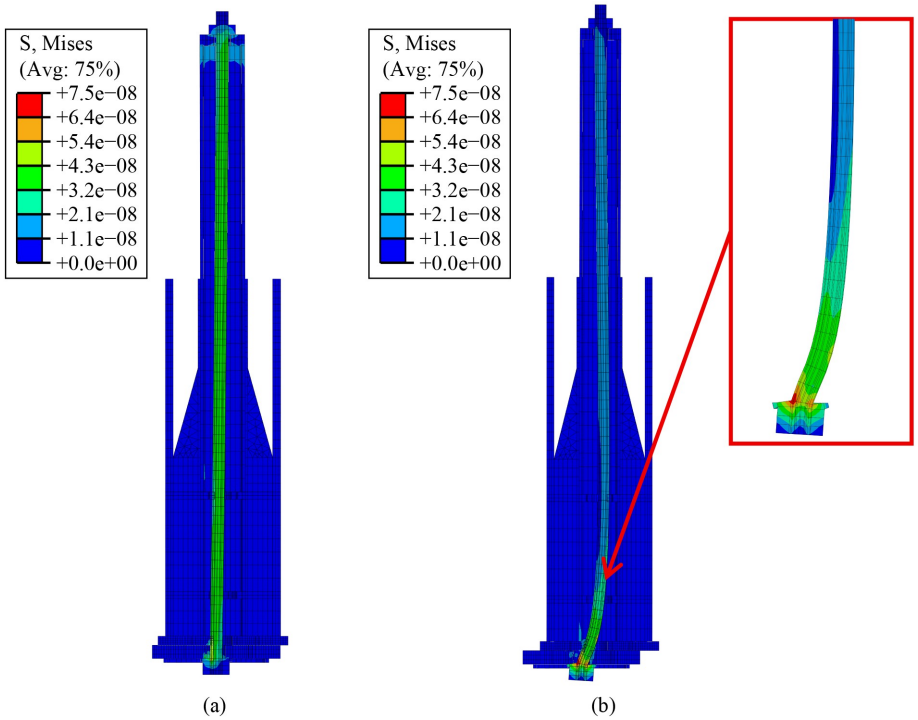


Fig. 22 von Mises of the model under the purified shear load: (a) before; (b) after collision.

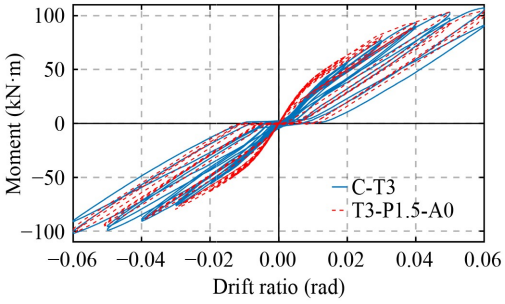


Fig. 23 Verification of the sample.

Through the structural analysis, the ceiling beam that is released at the end of the beams cannot bear any moment. Hence, it does not play any role in the structural behaviour, as shown by the moment and shear diagrams in Fig. 5. Although ignoring beams with simple connections is overestimated, the elimination of the ceiling beam in FE analysis and experimental test is close to the structural modelling.

To demonstrate that a ceiling beam with a simple connection has an insignificant effect on joint behaviour, model T3-P1.5-A0-1 was developed by adding a ceiling beam with a simple connection. A 150UB15.1 section was adopted, which is sufficiently strong to support the ceiling load and PE systems at the ceiling level of each module. The ceiling beam was connected to the column through web plates, and a vertical displacement, following the same pattern applied in other models, was imposed at the beam tip.

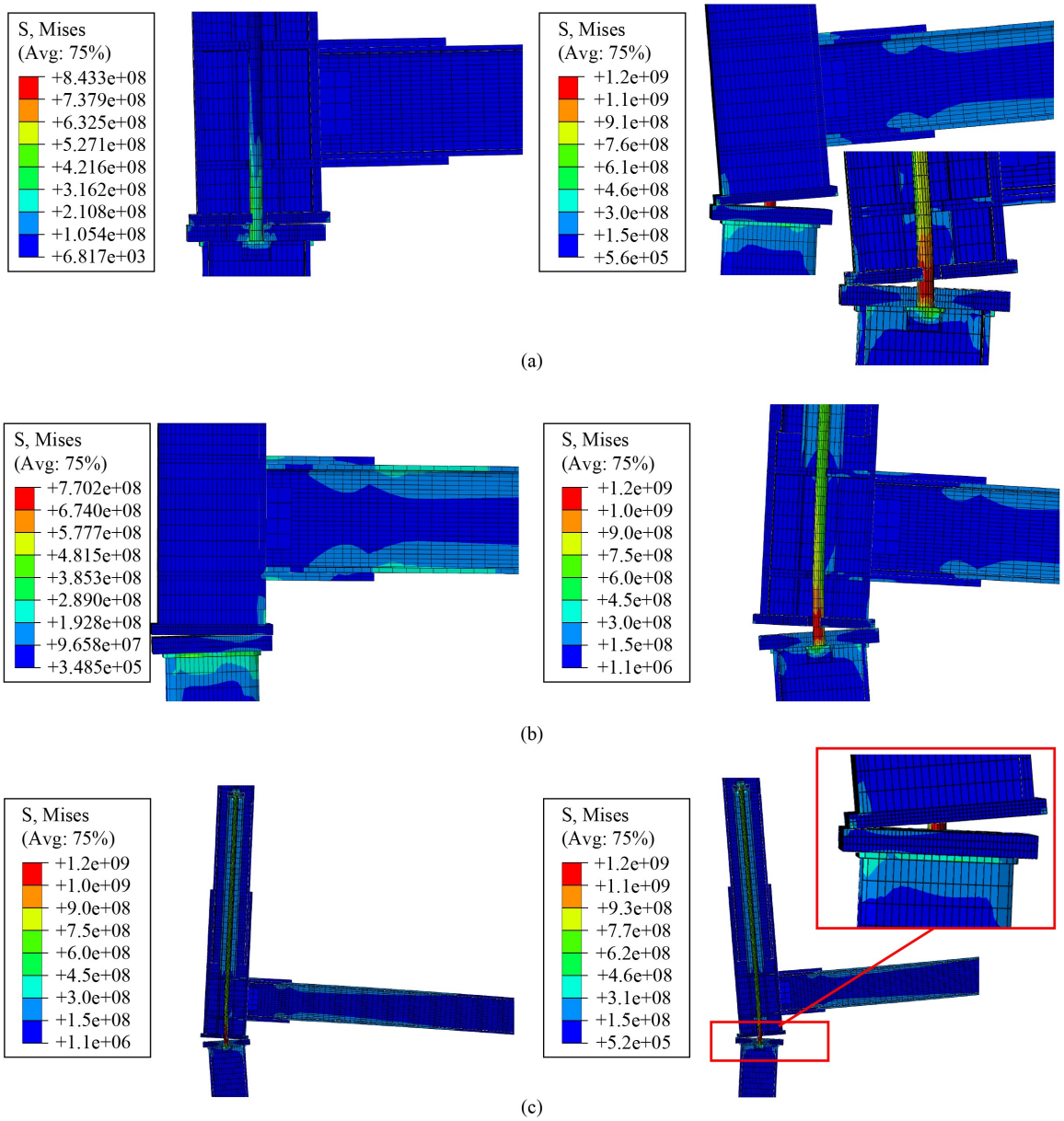


Fig. 24 Deformations in (a) initial opening; (b) sliding; (c) failure status in T3-P1.5-A0.

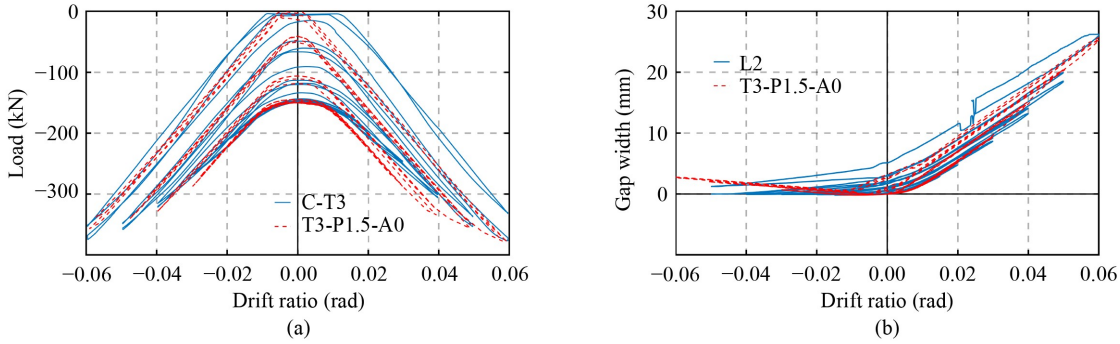


Fig. 25 FE results in (a) the rod's load; (b) the opening's width.

Figure 26 highlights the overall joint response, confirming that a ceiling beam with a simple connection has no appreciable effect on the joint's behaviour. Sliding was observed at a drift ratio of 5% during unloading.

A ceiling beam with a rigid connection contributes to moment distribution within a joint. This can reduce the moment transferred to the RSI. However, a ceiling beam with a simple connection has negligible moment capacity. The deformation pattern and plastic hinge formation are similar to those in model C-T3 (Fig. 27). The web plates, directly connected to the column sides, can develop tensile forces. Collars may be installed on both sides of the columns to control these tensions.

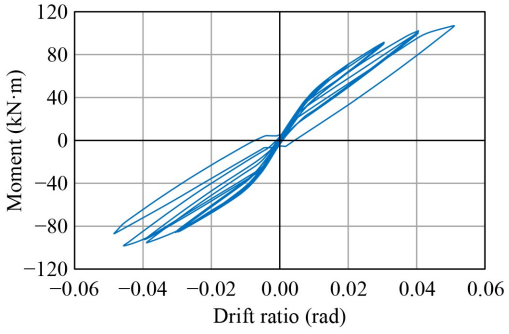


Fig. 26 The general behaviour of T3-P1.5-A0-1.

4.3 The effects of axial load in Rocking Steel Interconnection

The axial load from gravity and live loads influence the shear behaviour of the RSI, as described by Eq. (3). To evaluate this effect, models were analysed with axial loads equivalent to 5%, 10%, and 20% of the column's ultimate strength. It is assumed that these percentages represent axial loads occurring throughout the height of the column in the case-study building.

The results demonstrate that an increase in axial load increases frictional resistance, thereby preventing sliding. The shear resistance provided by the axial load is sufficient to ignore the effect of preload on the shear behaviour of the interconnection in all phases of

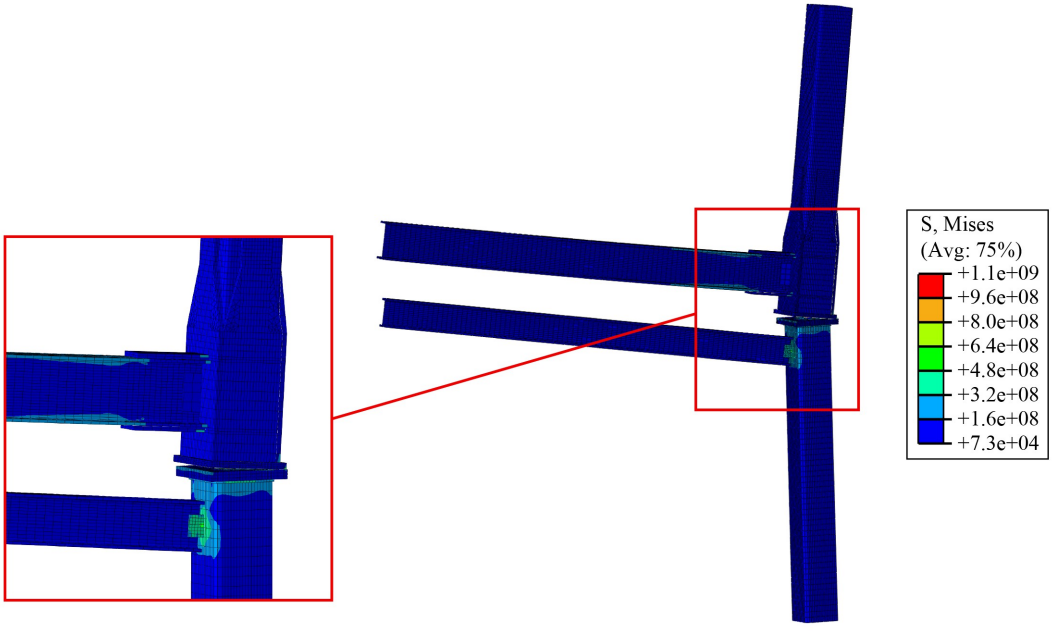


Fig. 27 Stress on the model T3-P1.5-A0-1 with simple ceiling beam-to-column connection.

deformation in the joint. Additionally, the increase in axial load also affects the moment behaviour of the RSI and its interaction with the intra-connection, as reflected in the cyclic behaviour shown in Figs. 28 and 29.

When the behaviour of the RSI dominates the joint's overall response, as shown by the behaviour of models without axial load in Figs. 28 and 29, pinching occurs in the cyclic behaviour. In contrast, cyclic behaviour with greater energy dissipation occurs when a plastic hinge forms within the intra-connection.

Axial load enhances the moment capacity of the RSI. On the other hand, P–Δ effects due to the axial load can negatively impact the moment capacity, particularly at large drifts when there is an opening. In models with lower axial loads, the likelihood of a large opening width increases. The opening causes out-of-line displacement of the column, resulting in P–Δ effects. However, when the RSI has no openings, P–Δ effects can be neglected because the column exhibits negligible out-of-line displacements. It should be noted, if the loading is

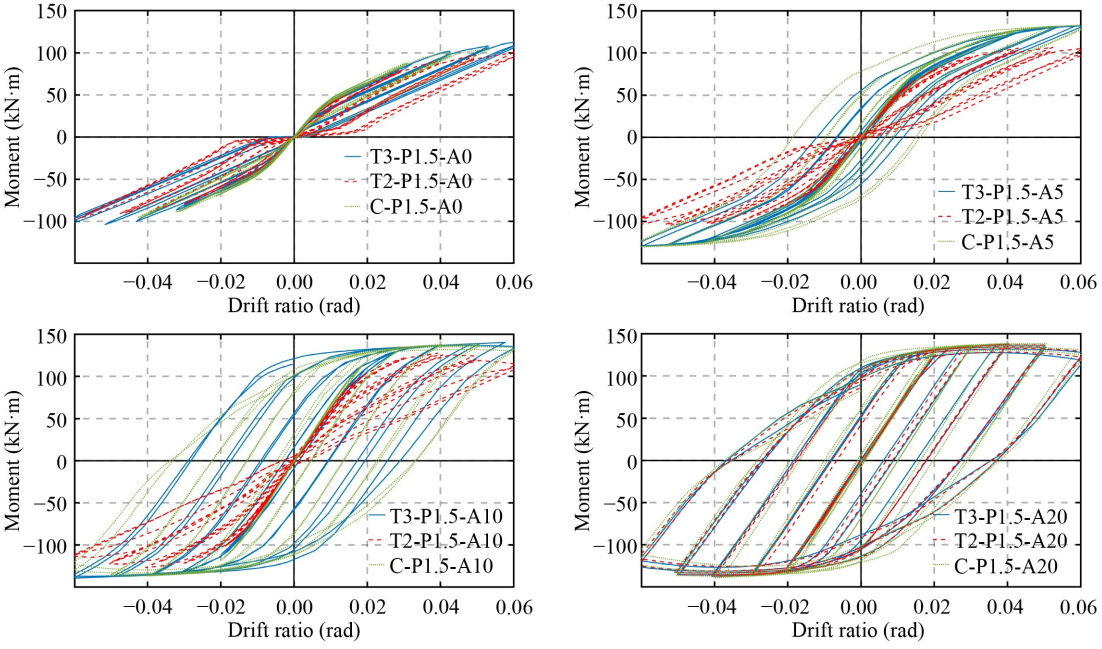


Fig. 28 Cyclic behaviours of RSI with a rod imposed 160 kN as a preload and various axial loads.

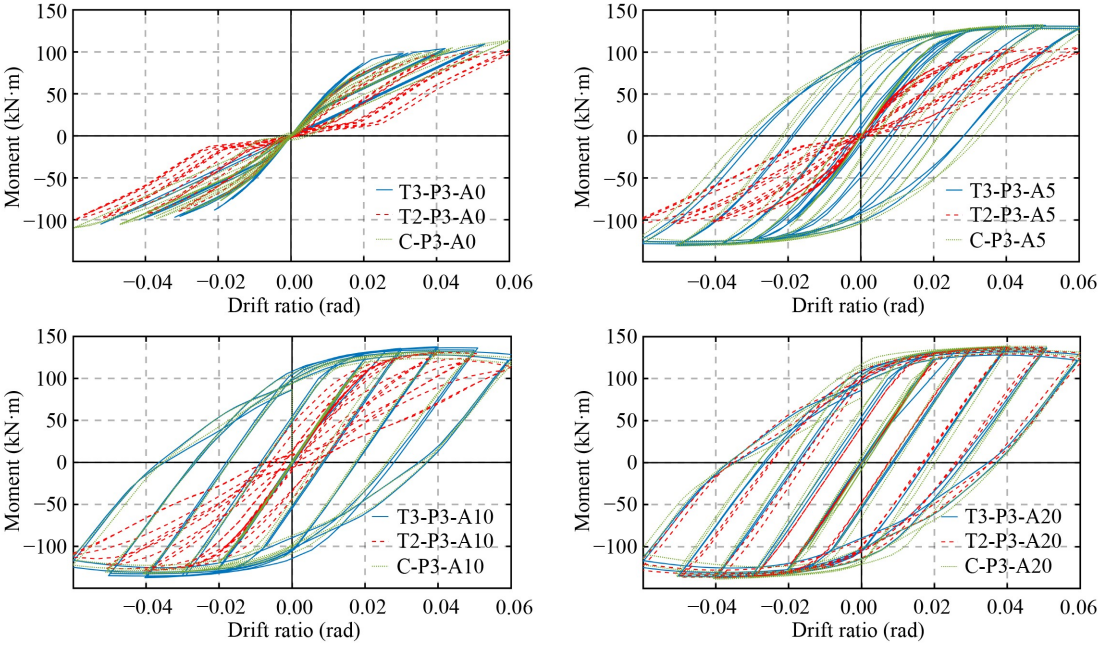


Fig. 29 Cyclic behaviour of the connection with the rod imposed 320 kN as a preload and various axial loads.

applied on the column laterally, the result be different as discussed in Ref. [59].

In models with 0% and 5% axial load, the RSI behaviour predominantly dominates the overall joint responses. As the out-of-plane loads through the column for all models with 0% axial load are the same, based on Fig. 30, it is expected that the cyclic behaviour will have a similar trend regardless of the plate thickness.

In models T3-P1.5-A10 and C-P1.5-A10, the application of a 10% axial load enhances the moment capacity of the RSI, surpassing half of the beam's capacity (refer to Section 2). This indicates the formation of a plastic hinge within the protected zone of the beam, resulting in a beam-dominated response during the cyclic loading. Therefore, the cyclic behaviour of models T3-P1.5-A10 and C-P1.5-A10 has a broader trend, as illustrated in Figs. 28 and 29. On the other hand, in model T2-P1.5-A10, a plastic hinge forms within the RSI, governing the joint's behaviour.

A comparison of models T2-P1.5-A10 and T3-P1.5-A10 in Fig. 30 reveals that using thicker endplates reduces the opening width and the resulting column bowing under axial load. The model T2-P1.5-A10, which has a greater opening than T3-P1.5-A10, showed larger bowing based on Fig. 30(b). In this scenario, the P–Δ effect decreases the RSI's capacity, which leads to the appearance of pinching behaviour in T2-P1.5-A10.

Another challenge in this study is the out-of-plane deformation of the lower endplate. Although the post-test inspection shows no deformation in the C-T3 endplate, precise deformation analysis should be obtained from FE models. To determine the out-of-plane deformation of the plate, the vertical displacements of three points along a diagonal line of the endplate were measured. The displacement difference between the two opposite corners was halved, and this value was subtracted from the displacement of the middle point to obtain the out-of-plane deformation of the lower endplates in Fig. 31. A negligible deformation is observed in models with 30-mm-thick endplates. However, the thinner plates (20 mm)

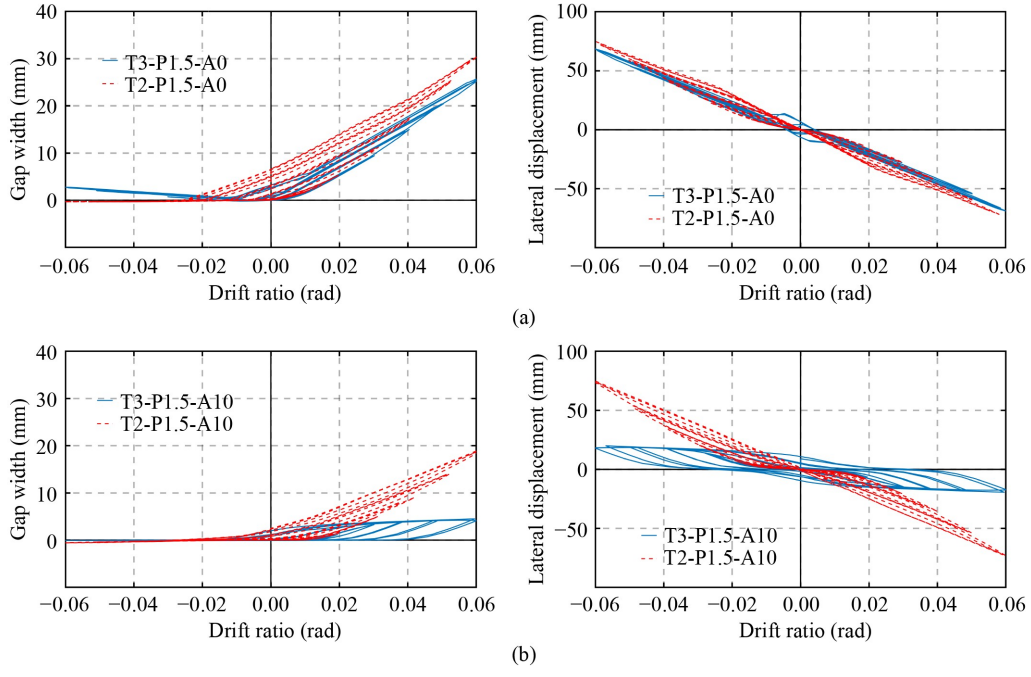


Fig. 30 The width of the opening and the lateral displacement of RSI in models with: (a) 0%; (b) 10% of axial load.

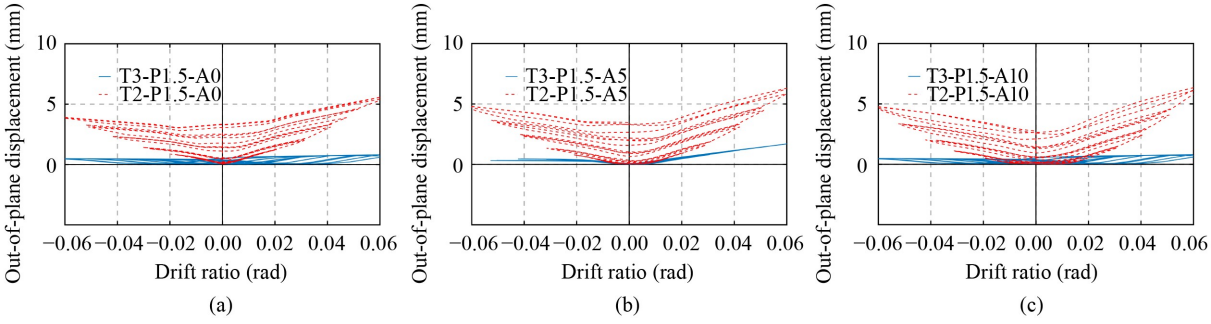


Fig. 31 Out-of-plane deformation for the end plate applied with: (a) 0%; (b) 5%; (c) 10% of axial load.

deform most at the centre when the model experiences the maximum drift in each cycle. When the load returns to zero, the out-of-plane deformation results in residual deformation in the endplate.

Regarding load degradation in the rods, Fig. 32 demonstrates that preload degradation depends on the width of the opening in the previous cycles. Additionally, if the lower endplate undergoes out-of-plane deformation due to the rod's pull-out load, this deformation reduces the rod's elongation in previous cycles. Specifically, in models T3-P3-A0 and T2-P3-A0 (Fig. 32(a)), the rods experience the same load at maximum drift within a cycle, but the load values at the unloading drift are different. The load at zero drift of each cycle in T3-P3-A0 decreases more significantly than in T2-P3-A0 due to the out-of-plane deformation in Fig. 31(a), which reduces the residual strain in the rod.

At an axial load of 20%, the RSI remains consistently close, resulting in the formation of a plastic hinge within the intra-connection, as illustrated in Fig. 33(a). Consequently, in models with 20% axial load, the rod is not expected to experience any degradation due to the absence of openings. The thickness of the endplate is not a significant factor. However, the presence of a lower collar is beneficial in reducing the likelihood of crippling in model T3-P1.5-A20 (Fig. 33(b)) compared to the von Mises tension observed in model C-P1.5-A20 (Fig. 33(c)).

5 Conclusions

This paper investigates the shear behaviour of RSI used in PPVCs. The previous research [38] examined the general (overall) behaviour and classification of RSI, finding that all components remained intact except for the rod and the lower endplate. In this study, a cyclic loading test was conducted to assess the cyclic behaviour of the RSI with a thicker endplate, designed to keep the lower endplate flat and intact. Additionally, the preload applied

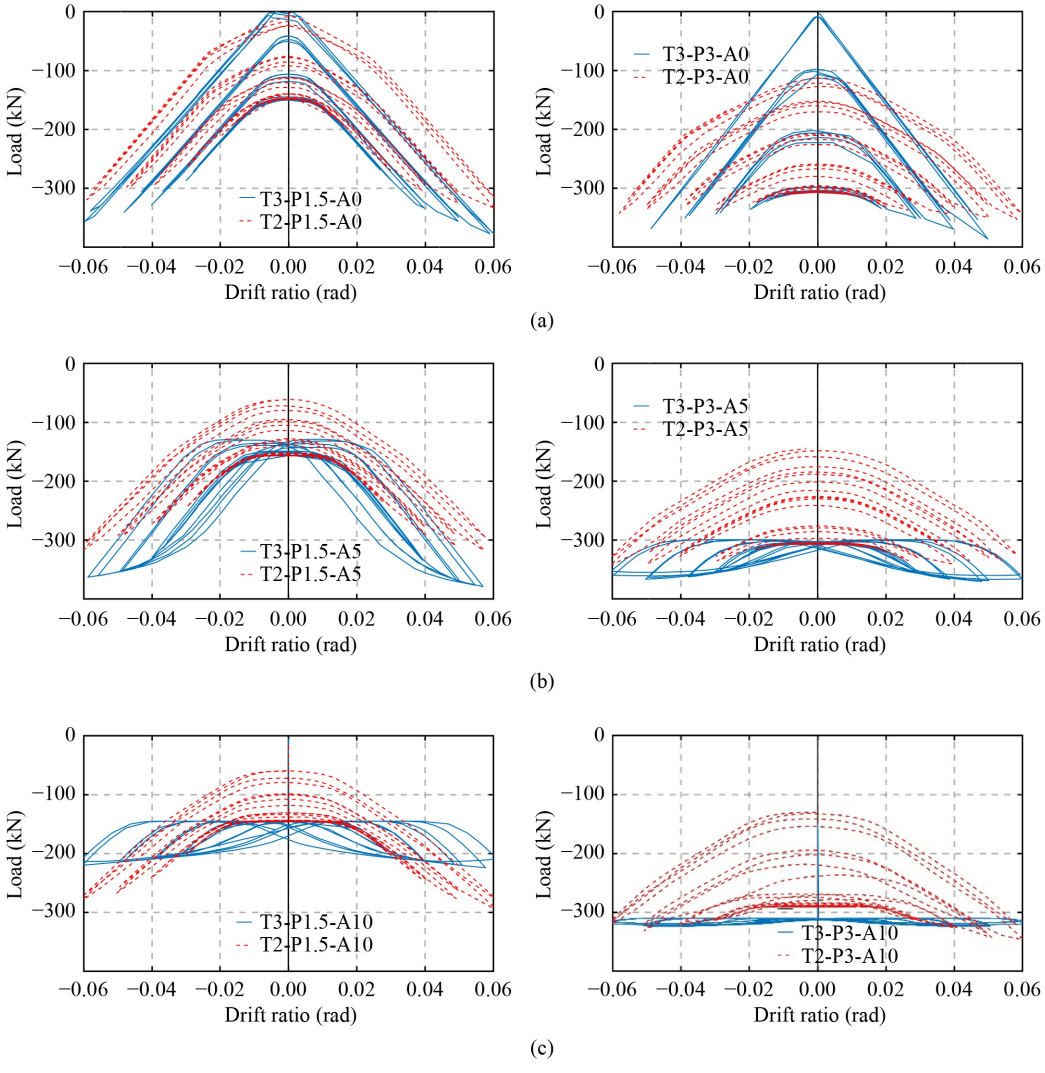


Fig. 32 Rod's load degradation in models applied with: (a) 0%; (b) 5%; (c) 10% of axial load.

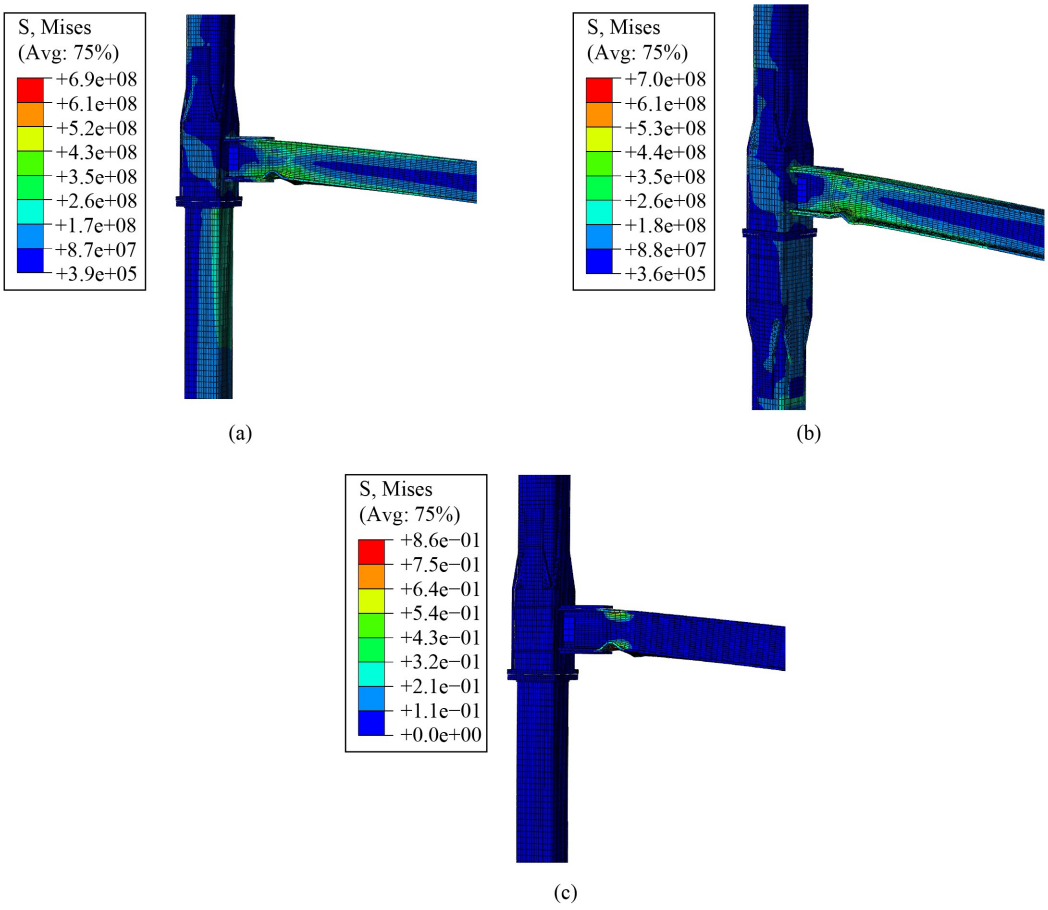


Fig. 33 (a) Plastic stress of T3-P1.5-A20; (b) von Mises stress and residual deformation of models T3-P1.5-A20; (c) C-P1.5-A10.

to the rod was reduced to half of the value used in the sample presented in Ref. [38], allowing for an assessment of the likelihood of sliding.

Lateral movement at the contact surface, observed in the test sample, was validated using ABAQUS software. The numerical model was then used (employed) to assess the effects of preload and axial load on the overall behaviour of the RSI. The FE analysis conducted on the joint yields the following key conclusions.

1) The thickness of the endplate and the preload value have a negligible impact on the overall moment behaviour of the tested joints. At the maximum drift of each cycle, the rod reaches its peak load, resulting in the highest moment in the interconnection.

2) The preload value affects the timing of joint opening, which coincides with the degradation of stiffness in the tested samples. Additionally, a correlation exists between load degradation in the rod and the opening width in the sample, as the opening generates residual strains in the rod.

3) Load degradation is unaffected by the preload value, as samples with varying preload values demonstrate similar load reduction. In the sample with a 160 kN preload, the rod load diminishes to nearly zero, enabling the shear load to exceed the frictional resistance and causing sliding.

4) Employing a thicker endplate enhances the joint's structural integrity under loading. No out-of-plane deformation was observed in the 30-mm-thick endplate, which effectively distributed the rod's pull-out load.

5) FE analysis reveals that either a 30-mm thick endplate or a lower collar in models 'C' provides comparable performance, both ensuring adequate rigidity to prevent out-of-plane deformation in the lower endplate.

6) In the sample with a 20-mm-thick endplate, the rod exhibits reduced load degradation due to deformations in the endplate. This behaviour suggests that the endplate and rod act as a series of springs, distributing residual strain between them. Consequently, part of the strain is absorbed by the plate, resulting in less residual deformation in the rod than in samples with endplates of greater rigidity.

7) The importance of preload in frictional resistance decreases in the presence of gravity loads. No sliding occurs in models subjected to axial load, even when the preload drops to zero in models with 5% axial load.

8) If the RSI remains closed due to axial load, the joint fails by forming a plastic hinge in the beam. For a non-sway joint subjected to axial load, the effects of P–Δ can be neglected when no opening appears in the RSI.

9) Out-of-plane deformation of the lower endplate in models with axial load, which experienced opening,

amplifies the out-of-line deformation of the column. This phenomenon further enhances the adverse effects of P–Δ.

Funding note Open Access funding enabled and organized by CAUL and its Member Institutions.

Open Access This article is licensed under a Creative Commons Attribution 4.0 International License (https://creativecommons.org/licenses/by/4.0/), which permits use, sharing, adaptation, distribution and reproduction in any medium or format, as long as you give appropriate credit to the original author(s) and the source, provide a link to the Creative Commons license, and indicate if changes were made. The images or other third party material in this article are included in the article's Creative Commons license, unless indicated otherwise in a credit line to the material. If material is not included in the article's Creative Commons license and your intended use is not permitted by statutory regulation or exceeds the permitted use, you will need to obtain permission directly from the copyright holder. To view a copy of this license, visit http://creativecommons.org/licenses/by/4.0/.

Competing interests The authors declare that they have no competing interests.

References

1. Li Z L, Guo Y T, Rao S H, Shang X Z, Noori M, Altabey W A, Farsangi E N, Zhu H T, Liu P Y. On the investigation of modular high-rise concrete buildings in the Asia Pacific region: Engineering application analysis and future directions. Results in Engineering, 2025, 26: 104830
2. Sharafi P, Samali B, Ronagh H, Ghodrat M. Automated spatial design of multi-story modular buildings using a unified matrix method. Automation in Construction, 2017, 82: 31–42
3. Sharafi P, Rashidi M, Samali B, Ronagh H, Mortazavi M. Identification of factors and decision analysis of the level of modularization in building construction. Journal of Architectural Engineering, 2018, 24(2): 04018010
4. McCord K H, Dillon H E, Hu A N, Carlson S, Phillips A R, Jung Y J, Gunderson P, Tarufelli B, Antonopoulos C A. Comparative life cycle assessment of a modular cross-laminated timber residential building designed for disassembly and reuse versus traditional wood frame construction. Journal of Cleaner Production, 2025, 528: 146541
5. Ahmed F, Gkantou M, Nikitas G, Ferentinou M, Bras A, Riley M. A review of recent developments in structural elements of modular steel building systems. Journal of Building Engineering, 2025, 111: 113087
6. Rajanayagam H, Poologanathan K, Gatheeshgar P, Varelis G E, Sherlock P, Nagaratnam B, Hackney P. A-state-of-the-art review on modular building connections. Structures, 2021, 34: 1903–1922
7. Srisangeerthanan S, Hashemi M J, Rajeev P, Gad E, Fernando S. Review of performance requirements for inter-module connections in multi-story modular buildings. Journal of Building Engineering, 2020, 28: 101087
8. Corfar D A, Tsavdaridis K D. A comprehensive review and classification of inter-module connections for hot-rolled steel modular building systems. Journal of Building Engineering, 2022, 50: 104006
9. Annan C D. Applicability of Traditional Design Procedures to Modular Steel Buildings. Dissertation for the Doctoral Degree. London: The University of Western Ontario, 2008
10. Huang Z Y, Zhao X L, Deng W X, Zhang W, Li T, Zhong Z Q. Flexural performance of high strength grouted SHS tube-sleeve connection for modular construction. Thin-Walled Structures, 2024, 198: 111653
11. Mou B, Li S Q, Song H T, Wu C L, Wang X J, Zhu Z, Yu H. Development and seismic performance assessment of welded connections in modular steel structures for high-rise buildings. Structures, 2025, 76: 108919
12. Ma R W, Xia J W, Chang H F, Xu B, Zhang L H. Experimental and numerical investigation of mechanical properties on novel modular connections with superimposed beams. Engineering Structures, 2021, 232: 111858
13. Lee S, Park J, Shon S, Kang C. Seismic performance evaluation of the ceiling-bracket-type modular joint with various bracket parameters. Journal of Constructional Steel Research, 2018, 150: 298–325
14. Chen Z H, Liu J D, Yu Y J, Zhou C H, Yan R J. Experimental study of an innovative modular steel building connection. Journal of Constructional Steel Research, 2017, 139: 69–82
15. Zhai S Y, Lyu Y F, Cao K, Li G Q, Wang W Y, Chen C. Experimental study on bolted-cover plate corner connections for column-supported modular steel buildings. Journal of Constructional Steel Research, 2022, 189: 107060
16. Zhai S Y, Lyu Y F, Cao K, Li G Q, Wang W Y, Chen C. Seismic behavior of an innovative bolted connection with dual-slot hole for modular steel buildings. Engineering Structures, 2023, 279: 115619
17. Park K S, Moon J, Lee S S, Bae K W, Roeder C W. Embedded steel column-to-foundation connection for a modular structural system. Engineering Structures, 2016, 110: 244–257
18. Styles A J, Luo F J, Bai Y, Murray-Parkes J B. Effects of joint rotational stiffness on structural responses of multi-story modular buildings. In: Proceedings of the International Conference on Smart Infrastructure and Construction. Westminster: ICE Publishing, 2016, 457–462
19. Farajian M, Sharafi P, Alembagheri M, Kildashti K, Bigdeli A. Effects of bolted connections' properties on natural dynamic characteristics of corner-supported modular steel buildings. Structures, 2022, 45: 1491–1515
20. Alembagheri M, Sharafi P, Hajirezaei R, Tao Z. Anti-collapse resistance mechanisms in corner-supported modular steel buildings. Journal of Constructional Steel Research, 2020, 170: 106083
21. Wang H, Feng R Q, Wang K L. Behavior and simplified calculation method of novel connections for assembled box-shaped steel structure. Advances in Structural Engineering, 2025, 28(11): 2055–2070
22. Liu J D, Chen Z H, Liu Y, Bai Y, Zhong X. Full-scale corner-supported modular steel structures with vertical inter-module connections under cyclic loading. Journal of Building Engineering,

2021, 44: 103269
23. Chen Z H, Wang J, Liu J D, Khan K. Seismic behavior and moment transfer capacity of an innovative self-locking inter-module connection for modular steel building. Engineering Structures, 2021, 245: 112978
24. Dai X M, Zong L, Ding Y, Li Z X. Experimental study on seismic behavior of a novel plug-in self-lock joint for modular steel construction. Engineering Structures, 2019, 181: 143–164
25. Yang N X, Xia J W, Chang H F, Zhang L H, Yang H. A novel plug-in self-locking inter-module connection for modular steel buildings. Thin-Walled Structures, 2023, 187: 110774
26. Srisangeerthanan S, Hashemi M J, Rajeev P, Gad E, Fernando S. Numerical study on performance assessment of an innovative boltless connection for modular building construction. Thin-Walled Structures, 2023, 185: 110622
27. Srisangeerthanan S, Javad Hashemi M, Rajeev P, Gad E, Fernando S. Development of an innovative boltless connection for multistory modular buildings. Journal of Structural Engineering, 2022, 148(7): 04022085
28. Zhang A L, Liu J D, Chen Z H, Chen T S. Bending behavior of detachable tapered-head bolt inter-module connection of steel modular structure. Journal of Constructional Steel Research, 2024, 220: 108829
29. Liu J D, Cao X Y, Yan S C, Chen Z H, Liu Y, Lu G N. Research on seismic behavior of tapered-head bolted inter-module connection of modular steel buildings. Engineering Structures, 2024, 304: 117586
30. Duan Y, Ping T Y, Young B, Pan W. Behaviour of an innovative inter-module connection system for high-rise steel modular buildings. Engineering Structures, 2025, 343: 121209
31. Atashfaraz B, Taiyari F, Sharafi P, Raad H H. Modelling rocking steel inter-module (RSI) connections: Parametric analysis of cyclic behavior and wind load performance. Structures, 2026, 89: 112222
32. Kujawa M, Smakosz Ł, Iwicki P, Perliński A, Tejchman J. Mechanical performance investigations of a post-tensioned inter-module connection in steel buildings. Structures, 2025, 71: 108187
33. Sanches R, Mercan O, Roberts B. Experimental investigations of vertical post-tensioned connection for modular steel structures. Engineering Structures, 2018, 175: 776–789
34. Lacey A W, Chen W S, Hao H, Bi K M, Tallowin F J. Shear behaviour of post-tensioned inter-module connection for modular steel buildings. Journal of Constructional Steel Research, 2019, 162: 105707
35. Lacey A W, Chen W S, Hao H, Bi K M. Simplified structural behaviours of post-tensioned inter-module connection for modular buildings. Journal of Constructional Steel Research, 2020, 175: 106347
36. Lee K, Rasmussen K J R, Cho B H. Bolt-free post-tensioned connection for steel-framed modular buildings and design for optimal preloading. Journal of Constructional Steel Research, 2024, 218: 108703
37. Lee K, Cho B H, Rasmussen K J R, Jung D. Experimental and numerical investigation of bolt-free preloaded connection for steel-framed modular buildings. Journal of Constructional Steel Research, 2024, 220: 108827
38. Atashfaraz B, Sharafi P, Shadan P, Goudarzi A. Rocking interconnection for moment resisting modular buildings: Experimental and numerical investigation. Journal of Constructional Steel Research, 2025, 224: 109139
39. Sharafi P, Atashfaraz B, Kildashti K. Novel rocking interconnection for superior prefabricated prefinished modular building system. Engineering Structures, 2025, 343: 120934
40. ANSI/AISC 358-22. Prequalified Connections for Special and Intermediate Steel Moment Frames for Seismic Applications. Chicago: American Institute of Steel Construction, 2022
41. ANSI/AISC 360-22. Specification for Structural Steel Buildings. Chicago: American Institute of Steel Construction, 2022
42. AS 4100-1998. Steel Structures. Sydney: Standards Australia, 1998
43. Lian J Y, Zhang W Y, Ding Y K, Lacey A W, Chen W S. Axial performance of a new self-locking and rapid-unlocking inter-module connection for modular steel construction. Thin-Walled Structures, 2025, 212: 113202
44. Farajian M, Kildashti K, Sharafi P, Eslamnia H. Quantification of seismic performance factors for modular corner-supported steel bracing system. Structures, 2022, 45: 257–274
45. Atashfaraz B, Sharafi P, Taiyari F. Seismic performance quantification of steel moment-resisting modular buildings considering structural details. The Structural Design of Tall and Special Buildings, 2025, 34(16): e70088
46. Alembagheri M, Sharafi P, Rashidi M. Experimental and numerical study on the robustness of full-scale volumetric steel module under sudden support removal scenarios. Journal of Performance of Constructed Facilities, 2022, 36(1): 04021112
47. Sharafi P, Alembagheri M, Kildashti K, Ganji H T. Gravity-induced progressive collapse response of precast corner-supported modular buildings. Journal of Architectural Engineering, 2021, 27(4): 04021031
48. Alembagheri M, Sharafi P, Tao Z, Hajirezaei R, Kildashti K. Robustness of multistory corner-supported modular steel frames against progressive collapse. The Structural Design of Tall and Special Buildings, 2021, 30(18): e1896
49. Hibbitt D, Karlsson B, Sorensen P. ABAQUS Standard Version 2021 User's Manuals. 2021
50. Shi Y J, Wang M, Wang Y Q. Analysis on shear behavior of high-strength bolts connection. International Journal of Steel Structures, 2011, 11(2): 203–213
51. Lacey A W, Chen W S, Hao H, Bi K M. Review of bolted inter-module connections in modular steel buildings. Journal of Building Engineering, 2019, 23: 207–219
52. AS/NZS 1170.0: 2002. Structural Design Actions, Part 0: General Principles. Sydney: Standards Australia/Standards New Zealand, 2002
53. AS/NZS 1170.1: 2002. Structural Design Actions, Part 1: Permanent, Imposed and Other Actions. Sydney: Standards Australia/ Standards New Zealand, 2002
54. Aryan H, Gencturk B, Hosseini F, Kavoura F. Evaluation of pinned column base-plate connections in low-rise metal buildings. Frontiers of Structural and Civil Engineering, 2025, 19(4): 578–597
55. ANSI/AISC 341-16. Seismic Provisions for Structural Steel Buildings. Chicago: American Institute of Steel Construction, 2016

56. Ban H Y, Shi G. A review of research on high-strength steel structures. Proceedings of the Institution of Civil Engineers-Structures and Buildings, 2018, 171(8): 625–641
57. Abbas J L, Allawi A A. Experimental and numerical investigations of composite concrete–steel plate shear walls subjected to axial load. Civil Engineering Journal, 2019, 5(11): 2402–2422
58. Wang L, Zhou S Y, Chen X S, Liu X, Liu S Y, Su D, Jiang S C, Zhu Q K, Yao H Y. Experimental and numerical investigation of the flexural performance of channel steel-bolt joint for prefabricated subway stations. Frontiers of Structural and Civil Engineering, 2024, 18(6): 918–935
59. Atashfaraz B, Sharafi P, Goudarzi A, Shadan P. Interaction of the rocking steel interconnection with intra-connections in a moment resisting modular joint. Engineering Structures, 2026, 365: 123230